



HDN of indole over Ir-modified Ti-SBA-15



Brenda C. Ledesma, Oscar A. Anunziata, Andrea R. Beltramone*

Centro de Investigación en Nanociencia y Nanotecnología (NANOTEC), Facultad Regional Córdoba, Universidad Tecnológica Nacional, Maestro López y Cruz Roja Argentina, 5016 Córdoba, Argentina

ARTICLE INFO

Article history:

Received 15 December 2015
Received in revised form 16 March 2016
Accepted 29 March 2016
Available online 30 March 2016

Keywords:

Hydrodenitrogenation
Titanium
Mesoporous
Iridium crystallites
Kinetic

ABSTRACT

The hydrodenitrogenation of indole has been studied over a series of Ti-modified SBA-15 supports and their respective Ir-catalysts. Ti-SBA-15 was synthesized using sol-gel method and Ti was added during the synthesis using Tetraethyl Orthotitanate. Iridium was added by wetness impregnation. The acidity of Ti-SBA-15 was modified adding F or Al in order to improve the catalytic activity. The catalysts prepared were extensively characterized by X-ray diffraction (XRD), N₂ adsorption isotherms, UV-vis-DRS, Raman spectroscopy, ²⁷Al-MAS-NMR spectroscopy, XPS, TEM-EDS, Py-FTIR, H₂-Chemisorption and TPR. UV-vis-DRS and Raman spectroscopy confirmed that Ti was incorporated in tetrahedral coordination in the framework of the SBA-15. The analysis showed that the mesoporous structure was maintained after F or Al incorporation. ²⁷Al-MAS-NMR spectroscopy indicated that aluminum was incorporated mainly in Td positions. The results showed that Ti incorporation helps to reduce significantly the size of iridium crystallites and improves its dispersion considerably. Ir/Ti-SBA-15 modified with Al, with Bronsted acidity, was the most active catalyst for indole HDN, in mild conditions in a Batch reactor. The experimental data for indole hydrodenitrogenation was quantitatively represented by a Langmuir–Hinshelwood type rate equation.

© 2016 Elsevier B.V. All rights reserved.

1. Introduction

Catalytic hydrotreating is an important process in petroleum refining used to remove about 90% of contaminants such as nitrogen, sulfur, oxygen and metals from liquid petroleum fractions. With air pollution regulations becoming more and more stringent, the interest in the hydrotreating process that comprises hydrodesulfurization (HDS) and hydrodenitrogenation (HDN) of diesel fuel has increased. The reduction of sulfur and nitrogen in the final product is of great importance from environmental point of view. Otherwise, it may convert into sulfur dioxide and nitrogen oxides which eventually can contribute to global warming as well as acid rain. Another important reason for sulfur and nitrogen removal is that they acts as a poison for the hydroprocessing catalysts and thus can lower the conversion. During hydrodesulfurization, sulfur is removed from the feedstock in the form of hydrogen sulfide and nitrogen in the form of ammonia. Hydrotreating is used before catalytic reforming and catalytic cracking to reduce sulfur and nitrogen and improve product yields, and to upgrade middle-distillate petroleum fractions into finished

kerosene, diesel fuel, and heating fuel oils. In addition, hydrotreating converts olefins and aromatics to saturated compounds. The content of nitrogen compounds is low compared to that of sulfur; hence little hydrogen is consumed by these reactions. However, some of the nitrogen compounds are difficult to convert. Indoles and carbazoles (non-basic nitrogen compounds) are the most predominant in AGO (ca. 300–400 ppm) and LCO (ca. 800–1000 ppm) [1–5].

Literature studies on the hydrodenitrogenation of five-membered heterocyclic compounds such as indole are less extensive [6–13], compared to those of six-membered ring such as quinoline and pyridine [14–17]. In addition, the kinetic information available for the hydrogenation of nitrogen compounds is mainly related to quinoline over NiMo/alumina catalyst.

Ni(Co)Mo(W)/alumina catalysts are commonly employed in the hydrotreating process. It is well known that the activity of transition metal strongly depends on the type of support employed since this interaction could determine the morphology, dispersion, sulfur lability, mobility and stability of the corresponding metallic site [18–20]. High surface area supports such as MCM-41 and SBAs [21–30], which display a uniform pore size distribution, have become potential candidates to host highly dispersed active phases and thus improve the catalytic performance with regard to the alumina catalytic support. Substituting the foreign ions (Al³⁺, Ti⁴⁺,

* Corresponding author.

E-mail addresses: abeltramone@frc.utn.edu.ar, lelitajones@hotmail.com (A.R. Beltramone).

Zr⁴⁺) into the silicate framework has proven an efficient route in order to enhance the acidity and stability of the mesoporous silica provided a better dispersion of Ni (Co) and Mo (W) species [31–36].

Noble metals such as Rh, Ir, Ru and Pt supported on silica or alumina are known to catalyze effectively nitrogen removal from methylamine, quinoline or pyridine, also in the reduced state [37–43]. These studies suggest that Ir could be an efficient active phase for transforming nitrogen compounds into hydrocarbons, either by itself or as a promoter of conventional catalysts.

The activity and selectivity of the catalyst is influenced by the following factors: the type of the metal used, the size of metal particles, the acidity and pore size of the support, the distance between metal and acid sites, and the reaction conditions (temperature, hydrogen pressure).

In our previous work [44], we observed that the presence of Ti-species on the surface of SBA-16 increased the strength of Ir interaction with the SBA-16-type support, leading to a more homogeneous distribution of Ir-species than on other pure silica support. The catalyst synthesized by us had good activity measured in tetralin hydrogenation in presence of quinoline. The expected higher activity of the iridium supported-mesoporous catalysts prepared here, compared with NiMo catalysts is ascribed to the high hydrogenation activity of the noble metal and the higher dispersion of the active phase that could be obtained using a mesoporous support with high surface area. Moreover, these noble metals can act as real active sites where the HDN reaction takes place. This is probably due to the greater number of sites of Ir acting as active hydrogen suppliers.

Thus, in this work, the reaction network and kinetic of indole HDN has been investigated over a series of Ti-modified SBA-15 supports and their respective Ir-catalysts in mild conditions. Iridium is chosen as hydrogenation catalyst and Ti-SBA-15 and Al or F modified Ti-SBA-15 are chosen as support with mild acidity. We expect that the Ir sites are responsible for aromatic saturation and hydrogenolysis, whereas the mild acid sites help to improve the C–N scission.

2. Experimental methods and materials

2.1. Synthesis of the catalysts

2.1.1. Synthesis of Ti-SBA-15

Ti-SBA-15 were synthesized using Tetraethylorthosilicate (TEOS, 98%, Sigma–Aldrich), Tetraethylorthotitanate (TEOT, 98% Sigma–Aldrich), Pluronic 123 in acidic medium. 9 g of P123 dissolved in 288 mL of HCl (2 M). The temperature of the P123 solution was controlled at 35 °C. After that, 20.1 mL of TEOS were added to the P123 solution under stirring for 20 min; 2.1 mL of TEOT were then added to the resultant solution and maintained in static condition for 24 h. The resultant mix was transferred into a Teflon bottle and maintained at 80 °C for 24 h without stirring. The sample was calcined at 550 °C for 5 h to remove the copolymer template. This sample with Si/Ti = 10 is here referred to as Ti-SBA-15.

2.1.2. Aluminum incorporation

Aluminum was incorporated by post-synthesis alumination. NaAlO₃ was dissolved in 50 mL of bi-distilled water. Ti-SBA-15, previously synthesized, was incorporated to the solution. The resultant mix was stirred during 24 h at 80 °C. Afterwards the solution was filtered and the solid was calcined during 5 h at 500 °C. Na was removed by ionic exchange with a solution of NH₄Cl, 1 M at 80 °C under stirring during 40 h. Then the sample was calcined at 500 °C. This sample with Si/Al = 20 is here referred to as HAl/Ti-SBA-15.

2.1.3. Fluorine incorporation

Fluorine was incorporated by the wet impregnation method. Ammonium fluoride was dissolved in 20 mL of bi-distilled water; Ti-SBA-15, previously synthesized, was added to the solution. The solution was then introduced into a vacuum rotary evaporator at 65 °C until fully dried. Resultant material was calcined during 5 h at 500 °C. This sample with 1 wt.% of fluorine is here referred to as F/Ti-SBA-15.

2.1.4. Iridium incorporation

Iridium nanoparticles were incorporated into each support by the wet impregnation method. Metal precursor (iridium acetylacetonate (Ir(acac)₃)) was dissolved in 20 mL of ethanol at 50 °C, the solution was placed in a vacuum rotary evaporator to remove excess of ethanol at about 60 °C and 60 rpm. The resulting material was dried at 50 °C for 24 h and calcined at 500 °C. Finally, the catalysts were reduced by heating at 4 °C/min in a H₂ stream to reach 470 °C and remained at this temperature for 5 h. The iridium load was 1 wt.% in all cases. These samples are here referred to as Ir/SBA-15, Ir/Ti-SBA-15, Ir/F/Ti-SBA-15 and Ir/HAl/Ti-SBA-15.

2.2. Characterization of the catalysts

XRD patterns were collected by using a continuous scan mode. The scan speed was 0.02° (2θ)/min in the Philips X'Pert PRO PANalytical diffractometer, operating with CuKα X-ray radiation (X-ray generator current and voltage set at 40 mA and 45 kV), using small divergence and scattering slits of 1/32 mm and a goniometer speed of 1.2° (2θ) min^{−1}. The scanning range was set between 0.5° and 5°. The sample was crushed previously and placed in an aluminum sample holder. Elemental analysis was performed by inductively coupled plasma-atomic emission spectroscopy (VISTA-MPX) operated with high frequency emission power of 1.5 kW and plasma airflow of 12.0 L/min. The surface area was determined by the BET method using a Micromeritics Chemisorb 2720 apparatus, equipped with a TCD detector, after degassing the samples with N₂ (25 mL/min) at 400 °C. TPR was performed using a Micromeritics Chemisorb 2720 apparatus, with a flow of 14 mL/min of 10 mol% of H₂/N₂ heating up 500 °C. N₂ adsorption/desorption isotherms at 77 K were measured on ASAP 2420 equipment after degassing the samples at 673 K, determining textural properties as surface area and pore volume; pore size distribution was estimated using Barrett, Joyner, and Halenda algorithm. Ultraviolet-visible diffuse reflectance spectroscopy (UV-vis-DRS) was used to evaluate the relative distribution of octahedrally- to tetrahedrally-coordinated Ti species in the samples. The spectra were recorded with a PerkinElmer Lambda 650 spectrophotometer equipped with a diffuse reflectance accessory. Raman spectrum was obtained from an InVia Reflex Raman microscope and spectrometer using a 532 nm diode laser excitation. X-ray Photoelectron Spectra (XPS) were obtained on a Microtech Multilab 3000 spectrometer, equipped with a hemispherical electron analyzer and MgKα (hν = 1253.6 eV) photon source. An estimated error of ±0.1 eV can be assumed for all measurements. Peak intensity was calculated from the respective peak areas after background subtraction and spectrum fitting by a combination of Gaussian/Lorentzian functions. TEM were recorded in a JEOL 2100F microscope operated with an accelerating voltage of 200 kV (point resolution of 0.19 nm); coupled with Energy dispersive X-ray spectroscopy (EDS). Solid state NMR spectra were taken on a BRUKER AVANCE II 300 spectrometer operating at 78.2 MHz for ²⁷Al. JASCO 5300 FTIR spectrometer was used for Py-FTIR measurements. A thermostated cell with a special NaBr window warmed up to 400 °C and 4.2 × 10^{−2} Torr during 2 h was employed to avoid possible sample hydration. The fingerprint of the samples was obtained using wafers of the samples in NaBr. Hydrogen Chemisorption characterization was performed in a Chemisorb 2720 Micromeritics.

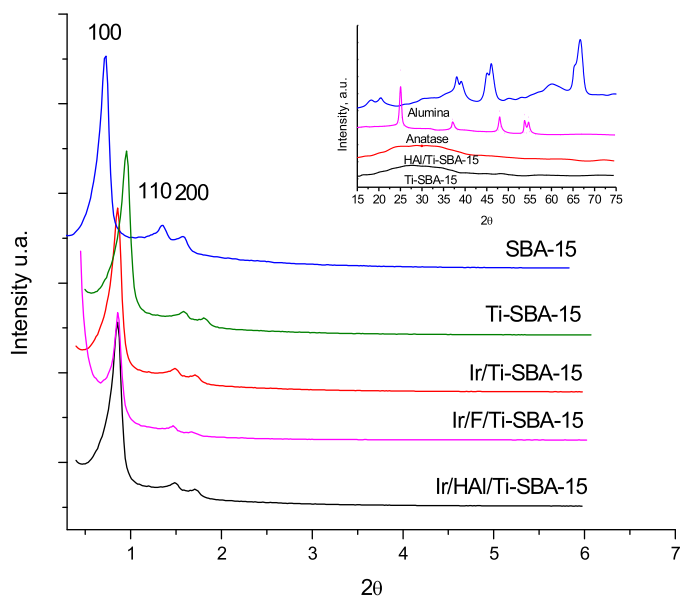


Fig. 1. XRD pattern of the samples synthesized.

The catalyst (0.5 g) was in situ reduced by H_2 (30 mL/min) at 400 °C for 2 h and purged by N_2 (25 mL/min) at 400 °C for an additional 0.5 h. The samples were cooled to 22 °C, and titrated by H_2 pulses in a stream of N_2 , until constant output TCD signal indicated saturation. The mean diameter of the Ir particles was estimated under the basic assumption of stoichiometry for $H/Ir = 2$, with spherical shape of the metal particles. The accuracy/reproducibility to the results is typically better than $\pm 1.5\%$ with $\pm 0.5\%$ reproducibility.

2.3. Catalytic activity

The hydrodenitrogenation reactions of indole were carried out at 250 °C and 15 atm of H_2 and 500 rpm in a 600 mL stirred autoclave (Parr Pressure Reactor 4536). The typical procedure was as follows: indole was dissolved in 50 mL of dodecane to a concentration of 0.01 M, equivalent to 150 ppm of N. The mixture was poured into the autoclave and the catalyst (250 mg) was transferred to the reactor. The reaction time was 8 h; samples were taken every hour. The results were compared with those of a typical HDN catalyst $NiMo/Al_2O_3$ Criterion DN200. This catalyst was presulfided according to [45]. The products were analyzed with a HP 5890 Series II GC and HP-5 capillary column and identified by GC/MS.

3. Results and discussion

3.1. Characterization of the catalysts

3.1.1. XRD

Fig. 1 shows the XRD plots of all the samples. Siliceous SBA-15 [46] materials showed three-peak pattern around $2\theta = 0.80$, 1.4 and 1.6, which are characteristic peaks of SBA-15 type mesoporous materials, representing the d_{100} , d_{110} and d_{200} planes with 2D hexagonal order of $p6mm$ symmetry structure. The peak position for Ir/Ti-SBA-15 slightly shifted to higher angles and the unit cell parameter (a_0) decreased from 12.04 nm for SBA-15 to 10.3 nm for Ir/Ti-SBA-15 (Table 1). The shift of unit cell parameter may be attributed to longer Ti–O bond length compared to Si–O bond. Such an observation indicates successful incorporation of Ti into SBA-15 structure.

In the wide-angle XRD pattern of the samples synthesized, between 15 and 80 2θ values (Inset, Fig. 1), we do not observe the characteristic peaks of anatase and/or alumina phase. The absence

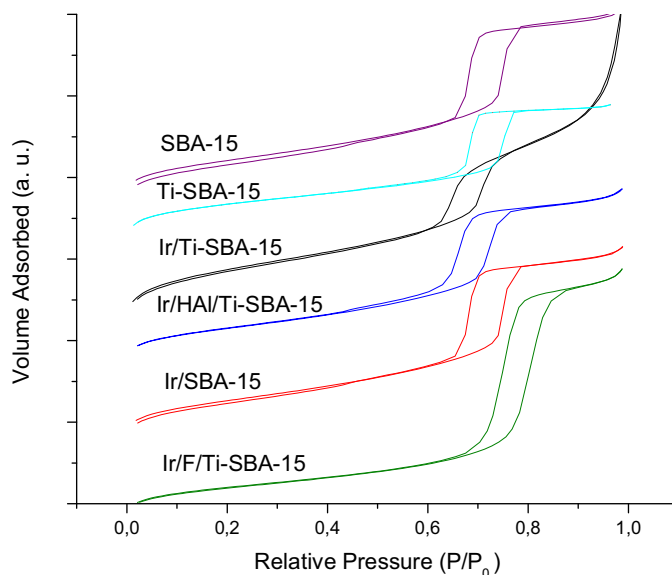


Fig. 2. N_2 adsorption–desorption isotherms of the samples synthesized.

of prominent reflections peaks indicates that no crystalline bulk material has been formed and Ti/or Al species are highly dispersed on the surface. This suggests that Ti and Al were incorporated mostly in tetrahedral position.

The iridium peaks (40–130 2θ ; not shown) are relatively broad due to the small size and high dispersed Ir nanoparticles, indicating that Ir particles could be formed inside SBA-15 during the inclusion process. The Ir nanocrystal size calculated according to the Scherrer diffraction formula ($d = jk/b \cos \theta$) was about 1.8 nm for Ir/Ti-SBA-15 sample.

3.1.2. N_2 adsorption–desorption isotherms and pore size distribution

The N_2 adsorption–desorption isotherms, pore size distribution and textural properties of Ti-SBA-15 doped with different metals are given in Fig. 2 and Table 1, respectively.

The isotherm of Ti-SBA-15 samples gives a clear H1-type hysteresis loop at a high relative pressure, suggesting that Ti-SBA-15 samples have very regular mesoporous channels despite their large pore size, proved by narrow Gaussian pore size distribution. These results indicate that the structure remains unchanged after Ti and Al addition, in agreement with XRD. Table 1 shows the pore diameter (d_p), pore volume (V_p) and specific area (SBET) of the supports. In all cases, the average pore size for Ir/Ti-SBA-15, Ir/HAl/Ti-SBA-15 and Ir/F/Ti-SBA-15 is quite similar and slightly higher than presented by the material support Ti-SBA-15, confirming that no pore blockage occurs after metal incorporation.

3.1.3. Raman spectroscopy

According to Fig. 3, three bands are observed for Ir/Ti-SBA-15 and Ir/HAl/Ti-SBA-15 at 490, 530 and 1100 cm^{-1} . The signals at lower frequency correspond to bending and symmetric stretching vibration of Ti–O–Si species in the framework, respectively. The band at 1100 cm^{-1} is attributed to the symmetric vibration of tetrahedral coordinated $[Ti(OSi)_4]$ units in SBA-15 [47].

Fig. 3, also shows the spectrum of Ir/F/Ti-SBA-15 and anatase used as a reference. The presence of the characteristic signals of anatase 403, 519 and 638 cm^{-1} [48], detected in the fluorinated sample demonstrates that at least some part of titanium changes to octahedral phase (NN = 6) after fluorination.

Table 1
Structural and textural properties of the catalysts.

	SBA-15	Ti-SBA-15	Ir/SBA-15	Ir/Ti-SBA-15	Ir/F/Ti-SBA-15	Ir/HAl/Ti-SBA-15
Area (m ² /g)	1050	898	740	679.9	350.8	407.9
a ₀	12.04	11.8	11.1	10.3	9.3	9.8
d _p (nm) ^a	6.5	6.4	6.3	6.76	7.5	6.78
V _p (cm ³ /gm) ^a	1.1	1.07	1.02	0.94	0.96	0.94
Ti (wt.%) (ICP) ^b	–	7.92	–	7.80	7.25	6.95
Ir (wt.%) (ICP) ^b	–	–	1.09	0.99	0.98	1.02
% metal dispersion ^c	–	–	60	92	80	89
Metal surface area (m ² /g) sample ^c	–	–	1.79	2.11	1.85	2.10
Particle diameter (nm) ^c	–	–	2.40	1.95	2.20	1.98

^a d_p pore diameter and V_p pore volume obtained by N₂-adsorption–desorption isotherms.

^b Data obtained by ICP.

^c Data obtained by Hydrogen chemisorption.

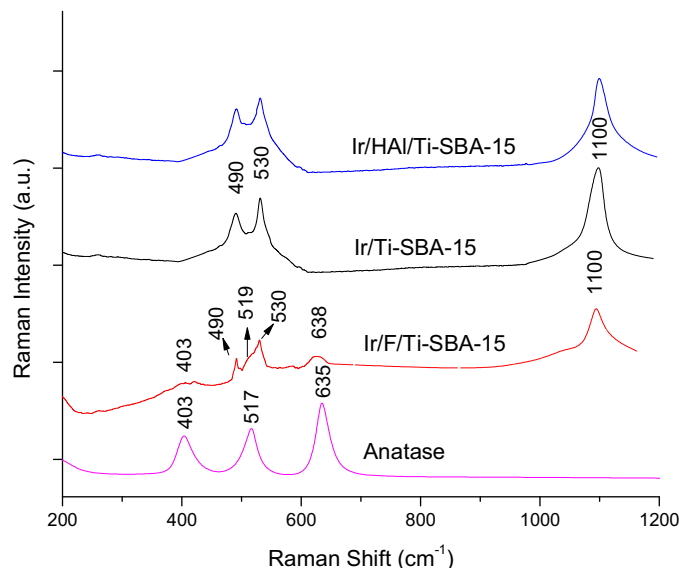


Fig. 3. Raman of Ti-synthesized samples. Anatase spectrum used as a reference.

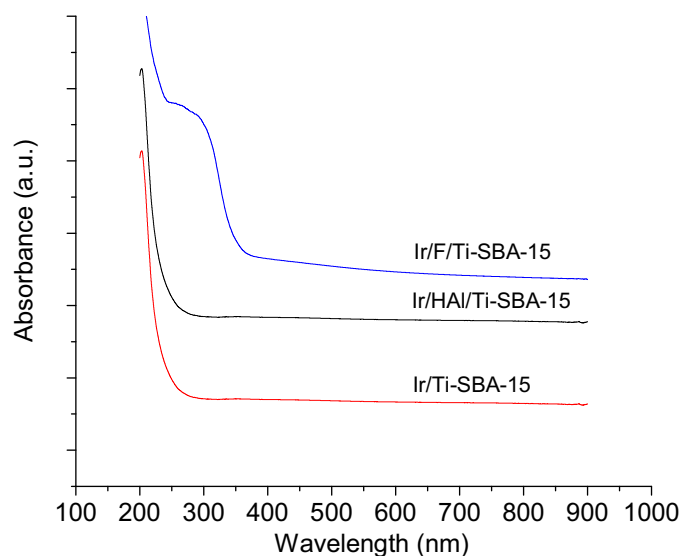


Fig. 4. UV-vis-DRS of Ti-synthesized samples.

3.1.4. UV-vis diffuse reflectance spectroscopic analysis

UV-vis diffuse reflectance spectroscopy (UV-vis-DRS) was used to study the dispersion and chemical environment of Ti incorporated in SBA-15 matrix. Fig. 4 shows the spectra of Ti-SBA-15 and Ti-SBA-15 modified with fluorine and aluminum. The band at

Table 2
Binding energies (eV) of core electrons of the samples synthesized.

	Si2p	O1s	Ti2p _{3/2}	F1s	Al2p	Ir4f _{7/2}
Ir/SBA-15	103.4	532.8	–	–	–	Ir ⁰ : 61.6 (80) ^a Ir ²⁺ : 64.3 (20)
Ir/HAl/Ti-SBA-15	103.4	532.8	459.5	–	75.2	Ir ⁰ : 61.7 (87) Ir ²⁺ : 64.4 (13)
Ir/F/Ti-SBA-15	103.4	532.8	458.6 (11) 459.4 (89)	687.4	–	Ir ⁰ : 60.1 (82) Ir ²⁺ : 61.5 (18)
Ir/Ti-SBA-15	103.4	532.8	459.5	–	–	Ir ⁰ : 60.7 (92) Ir ²⁺ : 61.7 (8)

^a wt.%.

210 nm, corresponding to tetragonal titanium with Ti(OSi)₄, structure is present in the three samples. The intense ligand-to-metal charge transfer transition band at ~200 nm (between titanium and oxygen in the framework pπ–dπ), attributed to mono-atomically dispersed Ti⁴⁺ ions in tetra-coordinated geometry, is the only band present in Ir/Ti-SBA-15 and Ir/HAl/Ti-SBA-15, clearly indicating that Ti ions are isolated and in tetrahedral (Td) coordination [49]. The results indicate that, in these samples, the Ti species introduced are well-dispersed in the SBA-15 mesoporous framework, in good agreement with what is determined from the wide-angle XRD patterns and Raman studies. The presence of an absorption band in the range of 240–330 nm suggests that some of the Ti ions occupy sites characteristic of extra-framework titanium. In the case of Ir/F/Ti-SBA-15 we observe a band at 240–330 nm corresponding to octahedrally coordination of Ti species [49–51]. Fluorine incorporation caused a shift of the absorption band to a higher wavelength range, indicating that some titanium has migrated from the framework to form TiO₂ particles. This is in agreement with Raman studies.

3.1.5. XPS

Binding energies (eV) of core electrons of iridium (4f signal) in Ir/Ti-SBA-15, Ir/HAl/Ti-SBA-15 and Ir/F/Ti-SBA 15 are shown in Fig. 5 and Table 2. According to the literature, BE at 61.0 eV is assigned to Ir⁰ and 62.0 eV is assigned to Ir–O. As seen in Fig. 5, a slight shift towards higher BE is observed, indicating the interaction of iridium dispersed species with the support [29,46,52,53].

Peak area analysis gives a major contribution of metallic Ir in Ir/Ti-SBA-15 sample; yet, in all the cases, Ir⁰ content is more than 80%, indicating that in all the samples most Ir are metallic atoms after the reduction procedure (Tables 2 and 3).

According to XPS spectra (not shown) and Table 2, the appearance of the signal of Ti2p_{3/2} at 459.4 (5) eV is indicative of tetrahedral Ti coordinated (NN=4) due to isomorphous Si substitution in all the samples, except the fluorinated sample. The shift to 458.5 eV in Ir/F/Ti-SBA-15 assigned to octahedral Ti (NN=6) [54], with a proportion of % 11, indicates that some part of the titanium

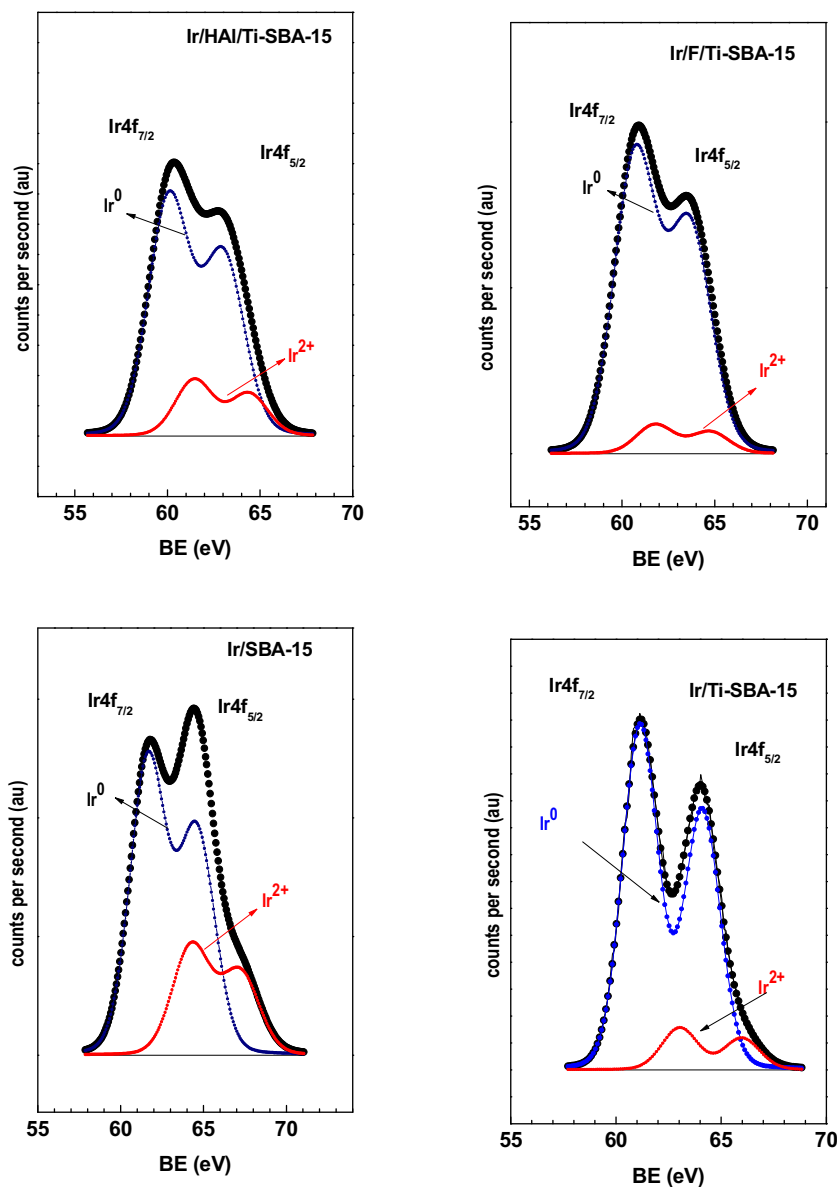


Fig. 5. XPS studies of Ir_{4f} of the samples synthesized.

Table 3

Atomic surface composition of the synthesized samples, obtained by XPS.

	Ti/Si (% at)	F/Si (% at)	Al/Si (% at)	Ir/Si (% at)
Ir/SBA-15	–	–	–	0.0074
Ir/HAl/Ti-SBA-15	0.0067	–	0.0036	0.0002
Ir/F/Ti-SBA-15	0.0053	0.0151	–	0.0002
Ir/Ti-SBA-15	0.0011	–	–	0.0001

atoms has increased the coordination number possibly due to the addition of fluorine. Thus, in agreement with the data obtained by UV–vis and Raman spectroscopy, most titanium is incorporated as Ti⁴⁺ isolated ions in tetrahedral (Td) coordination; however, in the case of the fluorinated sample, a portion of titanium is distorting the framework and/or in extra-framework positions. According to the atomic surface composition of the samples (Table 3) at 50–100 Å of depth (external surface of the catalysts), the atomic ratio (% at) are in the following order: Ir < Ti < Al < F in the corresponding samples.

The lower Ir content in the titanium synthesized samples indicates that the iridium crystallites could be in the internal surface of the structure. The high Al/Si ratio in Ir/HAl/Ti-SBA-15 suggests that

part of aluminum, added by post-synthesis procedure, is on the outer surface. However, the higher Ti/Si ratio in the sample with Al could be ascribed to Al incorporation in tetrahedral position in replacement of Si.

From the EDS results, the molar ratio of Ti/Si, Al/Si and Ir/Si was close to the initial synthesis conditions. For example in the case of Ir/HAl/Ti-SBA-15 we obtained: Ti/Si = 0.110, Al/Si = 0.482 and Ir/Si = 0.065. From XPS studies the molar ratio for this sample was: Ti/Si = 0.0017, Al/Si = 0.0026 and Ir/Si = 0.009. If they are compared with the values obtained by EDS, we can assume that most heteroatoms (Ti and Al) are in the framework and the metal coating (Ir) is in the inner surface of the catalysts. The same occurred in the other samples.

3.1.6. NMR-MAS

Fig. 6(a) shows the ²⁹Si-MAS-NMR spectra of Ir/HAl/Ti-SBA-15 sample. We observe a prominent peak at –111 ppm and a lower signal at –101 ppm, assigned to [Si(OSi)₄] (Q4) and [Si(OSi)₃OH] (Q3), respectively [55]. This analysis indicates that the incorporation of Ti

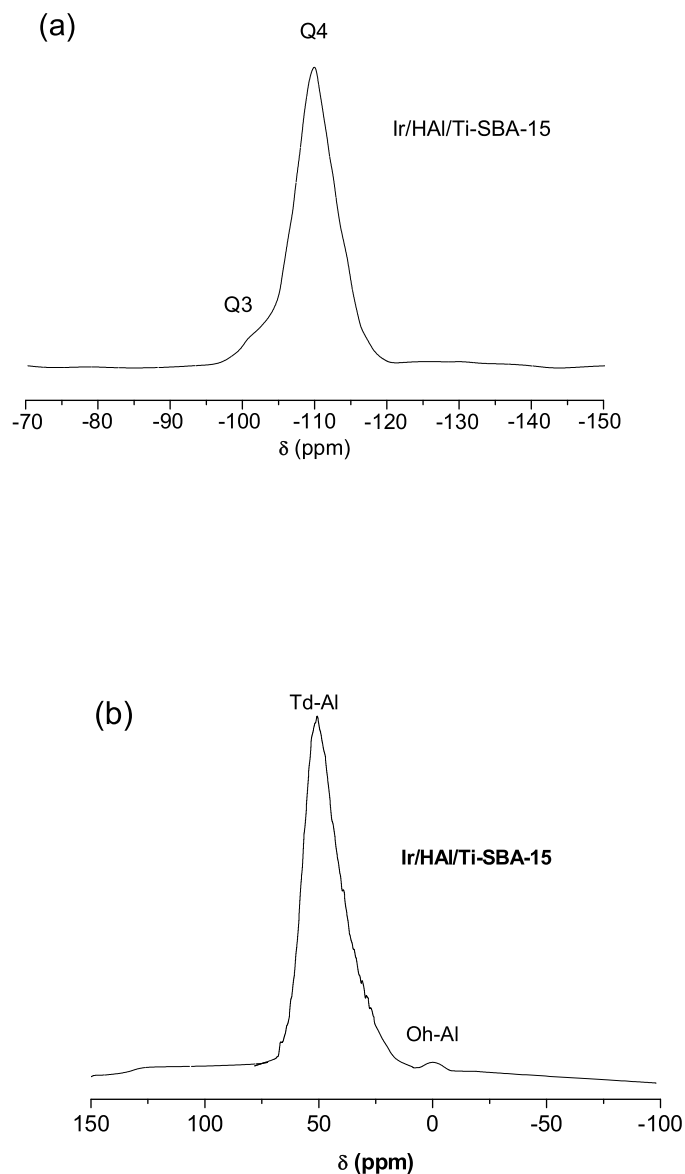


Fig. 6. (a) ^{29}Si and (b) ^{27}Al -MAS-NMR spectrum of Ir/HAl/Ti-SBA-15.

during the synthesis procedure followed by the post-alumination did not disturb the tetrahedral Si in the SBA-15 framework.

Fig. 6 The spectrum of ^{27}Al in Ir/HAl/Ti-SBA-15 showed in Fig. 6(b) exhibits peaks with chemical shifts of 0 ± 2 ppm and very low intensity assigned to octahedral-coordinated (Oh-Al) non-framework aluminum and another very intense signal at 50 ± 2 ppm assigned to tetrahedral-coordinated framework aluminum (Td-Al), suggesting that most of the Al is incorporated in tetrahedral coordination, even though there is some existence of extra framework Al-O-Si species in the material.

3.1.7. H_2 -Chemisorption

The dispersion and mean clusters sizes in the reduced catalysts are listed in Table 1. Lower particle size and higher dispersion of metallic iridium was obtained when Ti-SBA-15 support is used.

3.1.8. Py-FTIR spectroscopy

The acid strength of the Ti-SBA-15 supports was studied using the Pyridine adsorption method. Py-FTIR spectra of the Ti-SBA-15 samples were measured in the region of $1700\text{--}1400\text{ cm}^{-1}$. Results are shown in Table 4. According to the literature, pyridine adsorbed on Lewis acid sites exhibits signals at 1450, 1596 and 1615 cm^{-1} [56]. Bands at 1540 and 1640 cm^{-1} are assigned to Brønsted acid sites present in the material. Further, pyridine co-adsorbed on both Brønsted and Lewis acid sites gives rise to a band at 1495 cm^{-1} [57]. All catalysts exhibit Lewis acid sites, except HAl/Ti-SBA-15 that also shows high density of Brønsted acid sites. Py-FTIR results show that the incorporation of Al into the framework provides Brønsted acidity to the catalyst.

3.1.9. TEM

Morphology of the samples is observed via transmission electron micrographs (TEM). A typical hexagonal pore structure of SBA-15 materials with network channels, uniform pore size and long-range ordering was found. The TEM micrographs of the samples modified show no significant changes in catalyst morphology, suggesting that the metals are uniformly dispersed on SBA-15 support. From the TEM micrograph, the calculated pore diameter was about 7–8 nm, close to that estimated from nitrogen sorption isotherms. According to Fig. 7 iridium crystallites size is increased as follows: Ir/SBA-15 > Ir/F/Ti-SBA-15 > Ir/HAl/Ti-SBA-15 > Ir/Ti-SBA-15. This finding demonstrated that Ti incorporation helped to reduce the iridium crystallites size (1.8–2 nm) and improved the iridium dispersion.

3.1.10. TPR

The characterization of iridium catalysts is also carried out by temperature-programmed reduction; each spectrum provides information of the reducibility of the catalyst. TPR profiles plotted in Fig. 8 show the reduction temperatures for the samples synthesized. Ir/SBA-15 presents only one peak at 258°C . In the Ti-containing samples, reduction temperature of the iridium species decreases to 228°C , improving the reducibility of iridium. In the sample with Al incorporated via post-alumination method, reduction peaks occurred at slightly higher temperatures than those of Ir/SBA-15, probably due to a higher metal-support interaction present in a more acid support. All catalysts show only one peak; hence, they have similar Ir-species. These results are in agreement with those of previous studies reporting that higher reduction peak temperatures are indicative of stronger metal-support interactions [58,59]. Similar studies conducted in supported platinum precursors have shown that the strength of the platinum-support interactions varies as $\text{Al}_2\text{O}_3 > \text{SiO}_2 > \text{TiO}_2$ [60].

Table 4
Quantification of Brønsted and Lewis sites at different temperatures.

Temperature ($^\circ\text{C}$)	Ir/SBA-15		Ti/SBA-15		Ir/Ti-SBA-15		Ir/F/Ti-SBA-15		Ir/HAl/Ti-SBA-15	
	B (mmol/g)	L (mmol/g)	B (mmol/g)	L (mmol/g)	B (mmol/g)	L (mmol/g)	B (mmol/g)	L (mmol/g)	B (mmol/g)	L (mmol/g)
50 $^\circ\text{C}$	–	0.32	–	0.90	–	0.78	–	0.88	0.39	0.69
100 $^\circ\text{C}$	–	0.17	–	0.46	–	0.31	–	0.38	0.23	0.27
200 $^\circ\text{C}$	–	0	–	0.12	–	0.04	–	0.07	0.14	0.16
300 $^\circ\text{C}$	–	0	–	0.03	–	0	–	0.02	0.06	0.15

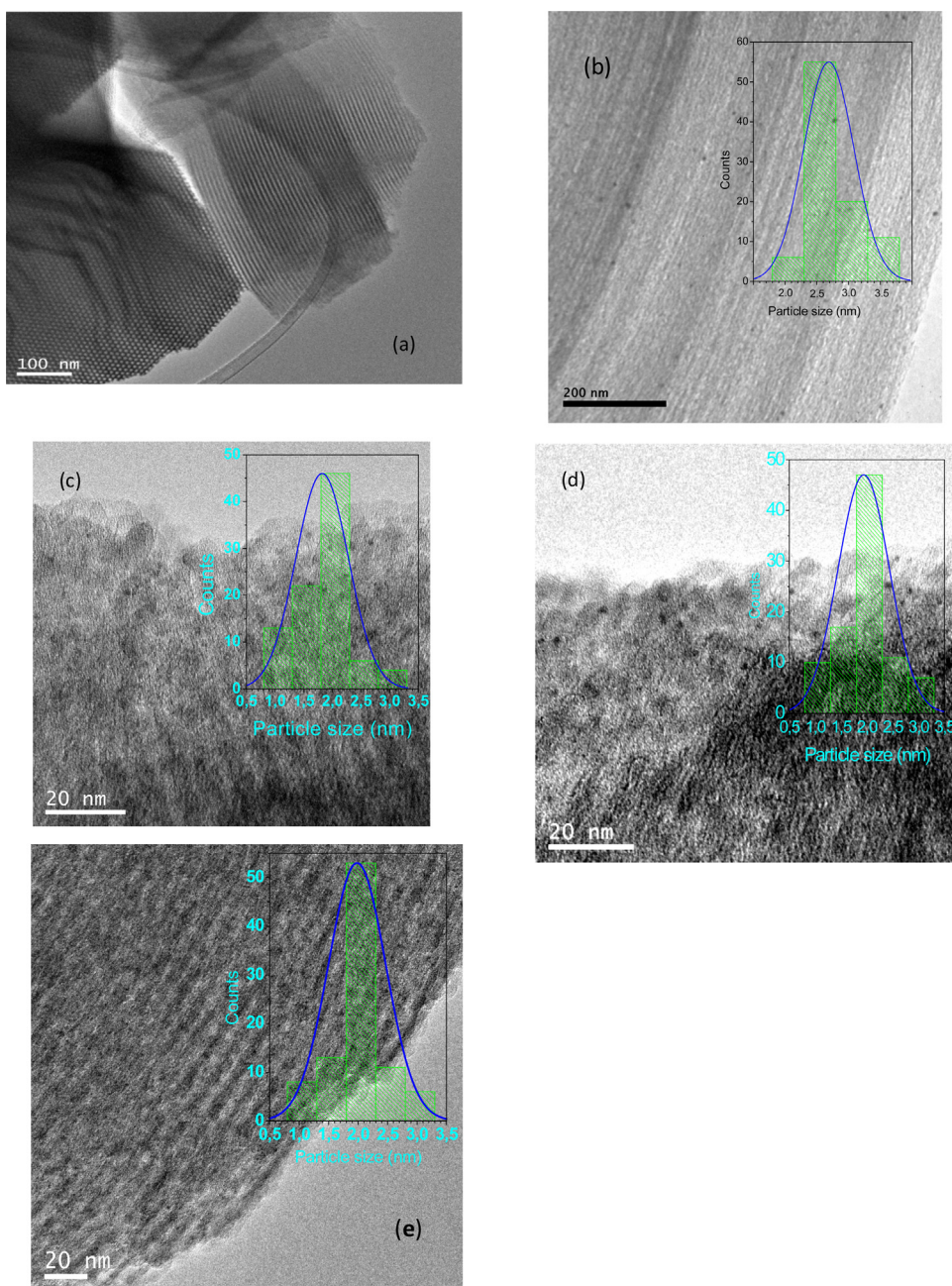
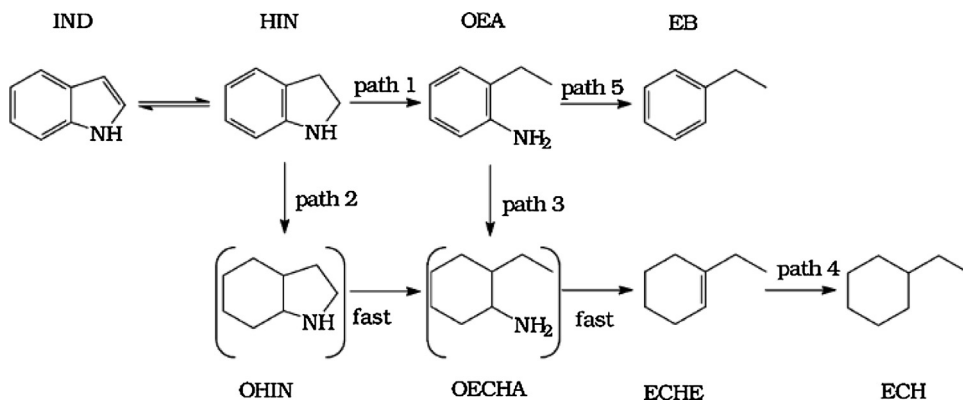


Fig. 7. TEM of (a) Ti-SBA-15; (b) Ir/SBA-15; (c) Ir/Ti-SBA-15; (d) Ir/HAl/Ti-SBA-15; (e) Ir/F/Ti-SBA-15.



Scheme 1. Reaction pathways for HDN of indole suggested by Zhang and Ozkan [57]. Indole (IND), indoline (HIN), *o*-ethylaniline (OEA), ethylbenzene (EB), octahydroindole (OHIN), *o*-ethylcyclohexylamine (OECHA), ethylcyclohexene (ECHE), ethylcyclohexane (ECH).

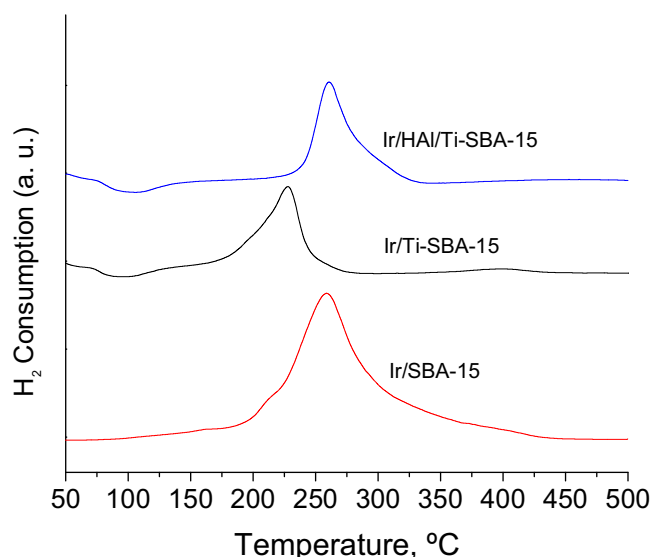


Fig. 8. TPR of the samples synthesized.

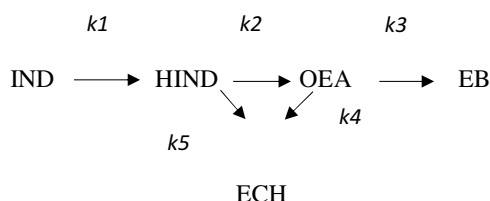
3.2. Catalytic activity

Scheme 1 shows the reaction network of indole HDN. Literature on indole HDN suggests that *o*-ethylaniline (OEA) is the exclusive intermediate towards formation of hydrocarbons [7,61–64], following indoline formation. Other studies [8] propose that the reactivity of OEA is negligible, so that denitrogenation of indoline is conducted via octahydroindole (OHIN), an intermediate from the complete hydrogenation of the benzene ring. However, OHIN has not been observed in any of the studies reported. Two major pathways were proposed to account for the formation of ethylcyclohexane (ECH) and ethylbenzene (EB), which are the two main HDN products from indole. One route occurs from hydrogenolysis of indoline (HIN) to *o*-ethylaniline (OEA) and the other from hydrogenation of indoline to octahydro-indole. A secondary route from *o*-ethylcyclohexylamine (OECHA) to ethylcyclohexene (ECHE) is also included in the mechanism proposed, occurring through a nucleophilic substitution reaction [33,65–67].

In several studies of indole HDN, ECH and EB were found to be the two major HDN products via OEA intermediate [7,62,63]. In previous works the hydrogenation of EB to ECH was found to be negligible [33,68].

In this work, the products identified by GC/MS were indoline (HIN), *o*-ethylaniline (OEA), ethylbenzene (EB) and ethylcyclohexane (ECH); these accounted for more than 95% of the total of the products. According to our experimental results and earlier findings from the literature [69,70], a modified indole HDN reaction network is proposed in Scheme 2.

The simplified reaction network takes into account 5 main reactions: (1) hydrogenation of indole to indoline, (2) hydrogenolysis of indoline to *o*-ethylaniline, and the simplified routes from (3)



Scheme 2. Simplified reaction pathways proposed for HDN of indole.

o-ethylaniline to ethylbenzene, (4) *o*-ethylaniline to ethylcyclohexane, and (5) indoline to ethylcyclohexane.

The hydrodenitrogenation reactions of indole were carried out at 250 °C and 15 atm of H₂ in a Parr reactor. The catalytic results revealed a good performance of Ir/HAl/Ti-SBA-15 and Ir/Ti-SBA-15; in both cases, indole conversion was higher than that obtained for Ir/SBA-15 and commercial NiMo catalyst. In order to compare the activity between the catalysts and to correlate it with the nature of the catalysts, the experimental data for hydrodenitrogenation of indole were quantitatively represented by a Langmuir–Hinshelwood type rate equation.

3.2.1. Control of the kinetic regime

A set of experiments was performed to check the absence of intraparticle and interphase mass transfer limitations. Different sizes of catalyst particles (0.2, 0.4, 0.6) were tested; the results indicated that in all cases a kinetic regime was established. External mass transfer limitation was evaluated changing the stirring speed ranging from 200 to 800 rpm to determine the effect of external mass transfer limitation. The rate of reaction increases initially with stirring speed and this rise is insignificant at or above 300 rpm, showing the independence of reaction rate from speed. Hence, all subsequent experiments were performed at 500 rpm.

3.2.2. Kinetic model

Under the conditions of the present study, all the reactions were considered irreversible, and since hydrogen is in excess, hydrogen partial pressure was considered constant; therefore, the resulting parameters were defined as apparent. The semi-empirical kinetic model proposed is the generalized Langmuir–Hinshelwood model [71–73]. After the simplifications, the reaction rate was given by:

$$r_{ij} = \frac{k_{ij}C_i}{\left(1 + \sum_m K_m C_m\right)^z} \quad (1)$$

Where r_{ij} (mol/Lh) is the rate of conversion of compound i to compound j , C (mol/L) is the concentration, k_{ij} (L/molh) is the apparent kinetic rate constant (including surface reaction and adsorption contributions) and K_m (L/mol) is the adsorption parameter of individual compounds. Z represents the number of surface sites required for reaction. The overall rate of production of a given compound was obtained from the summation of all the conversion rates involving species i . The rate parameters were regressed individually for each compound, with the constraint of non-negativity. As a first step, parameter estimation was performed using product distribution mole fraction (y_i) vs reactant conversion data involving a particular compound (y_i vs X_i) (Fig. 9). These relative rates eliminated the Langmuir–Hinshelwood Hougen–Watson (LHHW) denominators and provide the rate parameters for each step of the reaction (Eq. (2)). The numerator rate parameters k_{ij} , including surface reaction and adsorption contributions regressed by Eq. (2) were then held constant, and Eq. (1) was used for the estimation of adsorption parameters, K_m , using molar fraction vs time data (Fig. 10). The nonlinear parameter estimation of the kinetic model was performed with the Powell version of the Levenberg–Marquardt algorithm. The differential equation was solved using the EPISODE package of Scientist®. The objective function (Eq. (3)) was the sum of the squares of the differences between

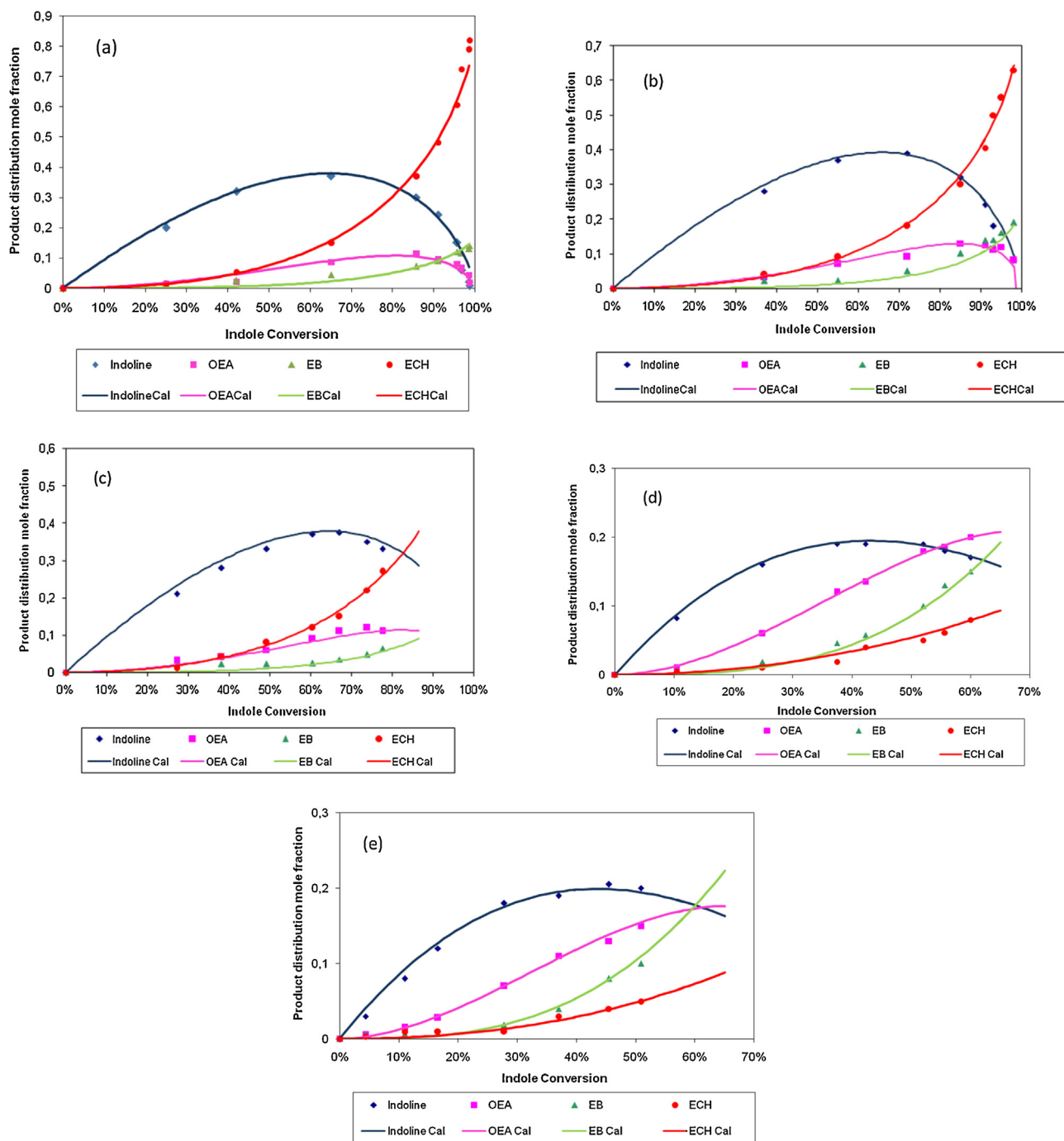


Fig. 9. Product distribution mole fraction of indole HDN (a) Ir/HAl/Ti-SBA-15 (b) Ir/Ti-SBA-15 (c) Ir/F/Ti-SBA-15 (d) Ir/SBA-15 (e) NiMo/Al₂O₃. The reaction time was 8 h; samples were taken every hour. The lines were obtained by fitting the kinetic curves derived from the model to the experimental data.

experimental and calculated mole fraction (y_i) of the products at different times.

$$\frac{d_{y_i}}{d_{x_i}} = \frac{\sum_j r_{ij}}{\sum_j r_{1j}} = \frac{\sum_j k_{ij} C_1}{\sum_j k_{1j} C_1} \quad (2)$$

$$F = \left(\sum_{i=1}^n y_{\text{exp}} - y_{\text{cal}} \right)^2 \quad (3)$$

From the figures, it is clear that the model allows describing the kinetics of the reactions. Tables 5 and 6 show the values of the reaction parameters and objective function for the simultaneous fitting.

The titanium-modified samples were much more active than those of Ir/SBA-15 and the commercial NiMo catalyst. Ir/HAl/Ti-SBA-15 had the highest production rate for all the paths, whereas ECH had the highest production rate from OEA, taking into account the highest value of k_4 . When hydrocarbon production of titanium-modified samples rates are compared, the most pronounced difference was found, in which the production rate of ECH increased significantly for Ir/HAl/Ti-SBA-15 and it became the

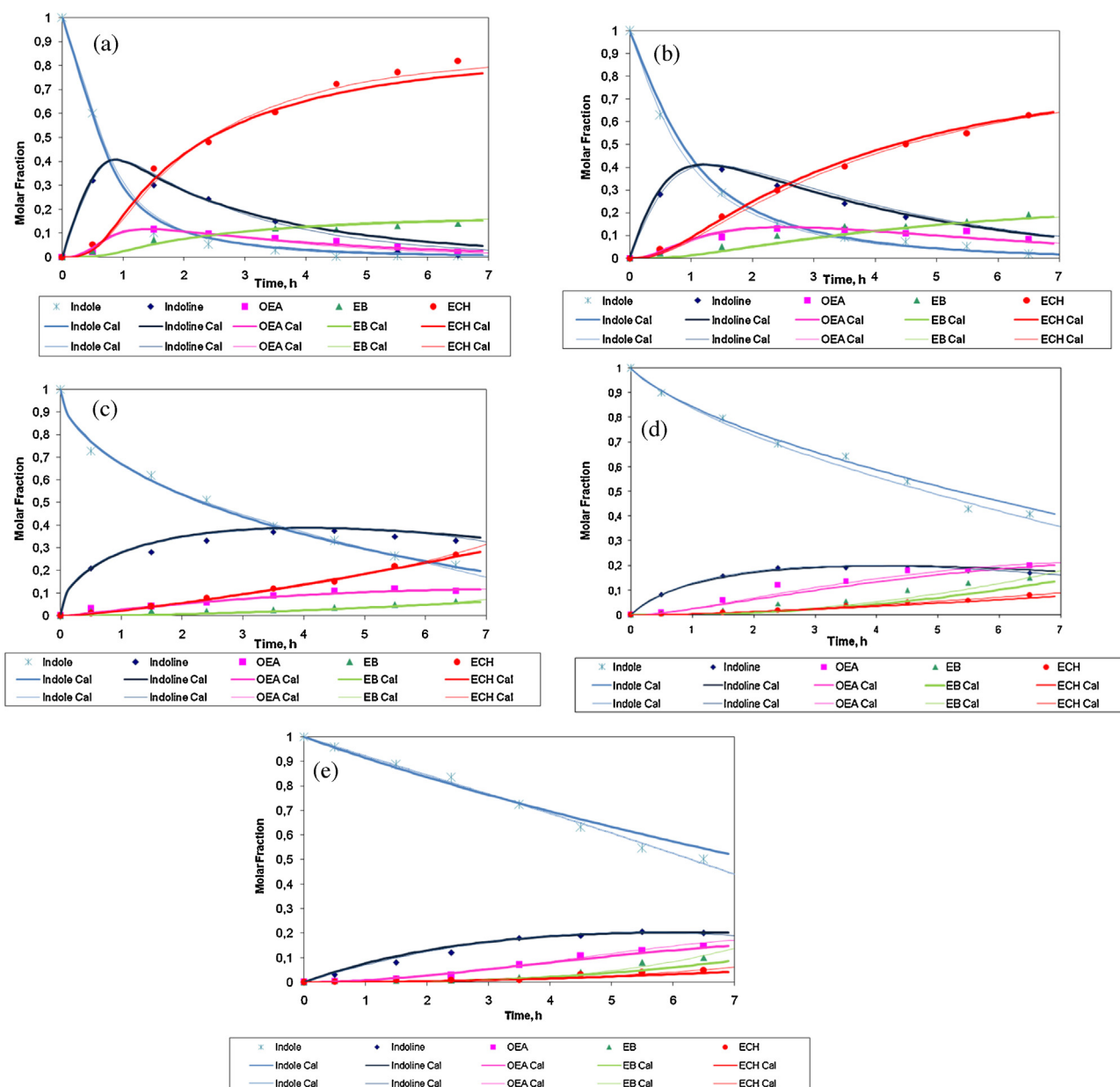


Fig. 10. Molar fraction vs time for indole HDN. (a) Ir/HAl/Ti-SBA-15 (b) Ir/Ti-SBA-15 (c) Ir/F/Ti-SBA-15 (d) Ir/SBA-15 (e) NiMo/Al₂O₃. The lines were obtained by fitting the kinetic curves derived from the model to the experimental data using $Z = 1$ thick line and $Z = 2$ thin line.

Table 5

Apparent kinetic rate constant obtained applying Eq. (2), according to the simplified pathway shown in Scheme 2. $F \leq 1 \times 10^{-3}$ in all cases.

Apparent kinetic rate constant (L/mol h)	NiMo/Al ₂ O ₃		Ir/SBA-15		Ir/Ti-SBA-15		Ir/F/Ti-SBA-15		Ir/HAl/Ti-SBA-15	
k_1	1.81		2.05		12.18		9.52		12.90	
k_2	4.60		2.54		6.50		5.40		7.93	
k_3	3.51		3.20		6.00		5.64		6.19	
k_4	0.66		0.40		10.05		9.45		18.25	
k_5	0.48		0.81		4.00		3.45		3.99	

Table 6

Adsorption constants (K) obtained applying Eq. (1), according to the simplified pathway shown in Scheme 2.

	NiMo/Al ₂ O ₃		Ir/SBA-15		Ir/Ti-SBA-15		Ir/F/Ti-SBA-15		Ir/HAl/Ti-SBA-15	
	Z = 1	Z = 2	Z = 1	Z = 2	Z = 1	Z = 2	Z = 1	Z = 1	Z = 1	Z = 2
	$F = 4.3 \times 10^{-3}$	$F = 0.9 \times 10^{-4}$	$F = 3.5 \times 10^{-3}$	$F = 0.5 \times 10^{-4}$	$F = 2.8 \times 10^{-3}$	$F = 9.8 \times 10^{-4}$	$F = 6.8 \times 10^{-3}$	$F = 2.1 \times 10^{-3}$	$F = 6.2 \times 10^{-3}$	$F = 1.2 \times 10^{-3}$
KIND	18	40	14	30	10	35	30	42	8	38
KHIND	20	55	22	58	39	100	47	102	37	95
KOEA	25	80	28	85	53	150	52	145	62	190

predominant product. On the other hand, EB was produced at lower rates than those of ECH.

Previous results using NiMo/Al₂O₃ showed that C–N bond cleavage reactions were relatively slow compared to hydrogenation reactions under the conditions studied [67]. In the case of our best catalyst, both hydrogenation and C–N bond cleavage were very fast compared with those of NiMo catalyst. This fact could be ascribed to the high hydrogenolysis capacity of iridium combined with Brønsted acidity generated by the presence of aluminum in the mesoporous framework. Hydrogenolysis reactions have higher activation energies than those of hydrogenation reactions and, the increase of the acidity will preferentially increase the rate of C–N bond cleavage reactions. OEA competes with indole for adsorption sites on the catalyst and it is primarily responsible for the formation of EB and ECH. All experimental results are consistent with those of the mechanism proposed. Titanium incorporation increases hydrogenation activity (*k*₁) more than six times compared with the sample without Ti and with a commercial NiMo catalyst. The HDN of OEA and HIND was highly increased with the presence of titanium, this could be due to better dispersion and good reducibility of iridium [29], combined with the presence of Lewis acidity of the support, which yields a more active catalyst. According to *k* values from Table 5, the yield for the saturation of indole did not change when Aluminum is added in the support, only HDN of OEA (*k*₄) was promoted by the stronger acidity resulting from post-alumination and further proton exchange. Fluorine incorporation did not improve HDN activity for Ir/F/Ti-SBA-15 catalyst; it indeed led to a slight decrease in HDN activity. This was probably due to the additional calcination step during preparation, causing, probably, some structural distortion. This could also be attributed to the too high concentration of fluorine, resulting in loss of area and structure. This effect was also observed with Rh/Al₂O₃ [74] in HDN of methylcyclohexylamine. A further study is required to determine this fact.

The determination of the adsorption constants for the different nitrogen compounds involved in the proposed mechanism (Eq. (1)) could help us to understand the different activities between the catalysts. In view of the differences among reactions taking place in the HDN network of indole, more than one type of catalyst site could be adequate (*Z* value). Kim et al. [13] assumed a three sites Langmuir–Hinshelwood rate model in the kinetic modeling of the HDN of indole over NiMo catalysts. Two types of sites were designated according Scheme 1, a CNH site (S₁) for IND to OEA (path 1) and a HYD site (S₂) for IND to ECHE (path 2) and for OEA to ECHE (path 3), because path 2 and 3 involve hydrogenation. Another site (S₃) was assumed for ECHE to ECH (path 4). Finally, OEA to EB (path 5) was assumed to occur on site S₁, as CNH is involved. This led to different adsorption constants for each step. They found that the different behaviors of the hydrogenation and hydrogenolysis functionalities are associated with different catalyst sites and the hydrogenation site is more susceptible to deactivation than the hydrogenolysis site. They found in the kinetic analysis that using a power of 1 for the inhibition (denominator) terms in the rate expressions (*Z* = 1) gave poor fits to the data, thus, the application of the square of the inhibition terms in the kinetic equations gave a better fitting. This may be rationalized by reaction of the adsorbed reactant species either with a vacancy site or with adsorbed H₂ or H on an adjacent site. Hadjilouzou et al. [75] reported that, in the HDN of pyridine, catalyst deactivation occurred in two distinct regimes, a rapid initial step followed by a more gradual activity decline. They attributed this to the deactivation of two types of catalyst sites with different activities. An additional complicating factor for reactions involving the formation of various intermediates is that these intermediates may have different adsorption constants. Depending on the strength of adsorption, it may be possible to omit some of the

parameters which model. For example, the adsorption of ECH and EB are weak and can be neglected in the rate equations.

Therefore, the distinction was made between these catalytic sites in the kinetic modeling applied in this work. Also, to simplify the kinetic calculations, it was assumed that *Z* could vary from 1 to 3. Rate equations were developed for each catalyst. Initial trials showed that assuming three type of active site, that is *Z* = 3, fit the data poorly. The very small amount of data was not sufficient to accurately model this assumption. Kinetic parameters were regressed using *Z* = 1 (one site) and *Z* = 2 (two sites). The data correlation is shown in Fig. 10, comparing experimental versus predicted mole fractions. The values are listed in Table 6.

According to de *F* values using *Z* = 2, the model fit well than with *Z* = 1, even when both fitting are very good (*F* < 1 × 10^{−3}), the existence of two active sites to describe the mechanism has more physical meaning. Iridium sites and the Lewis or Brønsted sites could be involve as separated sites for hydrogenation and hydrogenolysis. Regardless the fact that the mechanism of these catalysts should be different than for the NiMo catalyst, the higher activity could be explained in terms of the promotional effect of Brønsted sites and high dispersion of the active metal.

In Fig. 10, we observe that indole is quickly converted into indoline and *o*-ethylaniline, which are more basic compounds and possess higher adsorption constants (Table 6). The adsorption constants increases, for all the catalysts, in the following order: IND < HIND < OEA. The higher values were obtained for the more Ir/HAl/Ti-SBA-15. The basic and non-basic organonitrogen compounds have distinct electronic structures and properties that determine their HDN reactivities [76,77]. Therefore, the relative hydrogenation reactivity of basic and non-basic nitrogen compounds may vary depending on the electronic structures and properties of catalyst surfaces. Basic nitrogen compounds may show higher adsorption constant on acid surface, as is the case of HIND and OEA over our more acidic catalyst. The difference between the adsorption constants found applying this model suggests that HDN behavior seems to be related to the adsorption strength of the specific nitrogen compound on the catalyst surface. OEA has the higher adsorption constant for Ir/HAl/Ti-SBA-15 and also the higher rate for C–N bond cleavage to give ECH (*k*₄). This in agreement with Kim et al. [13] they found a stronger adsorption constant for the CNH site.

Indole non-basic could be adsorbed through weaker adsorption by the aromatic ring (π –adsorption mode) and the basic-intermediates through the nitrogen atom (σ –adsorption mode).

In a previous paper, Kim et al. [78] postulated that adsorption on site 1 (CNH path) was through the *N*-atom and on site 2 (HYD path) via π bonding of the aromatic ring. From theoretical calculations, Ruette et al. [79] showed both σ and π –adsorption modes are possible for pyridine adsorbed on a model MoS system. The kinetic results indicated that the majority of the C–N bond cleavage reactions in the HDN of indole takes place through C(sp³)-*N* bond cleavage. There can be two ways that C(sp³)-*N* bond cleavage can occur, that is, elimination and hydrogenolysis. By studying a series of amines, Portefaix et al. [80] demonstrated that an E2Hoffman-type elimination mechanism is responsible for the C–N bond cleavage in molecules which contain hydrogen atoms in the β -C position. It has been shown that the removal of NH₃ from aliphatic amines with hydrogen atoms on the carbon atoms in the β position is easy and that the rate is higher for molecules with more β -H atoms. Jian et al. [81] suggested that direct C(sp²)-*N* bond cleavage takes place on a different catalytic site than hydrogenation reactions in the catalytic hydroprocessing over sulfided NiMo/Al₂O₃ catalysts. The Hofmann elimination takes only place after quaternisation of the nitrogen atom by protonation by a Brønsted acid site creating a better leaving group. Two neighbouring sites are necessary, a Brønsted or a Lewis acid site to create

a better leaving group and a basic site to help remove the β -hydrogen atom. In our case, the aluminated support increases the Brønsted acidity of the Ir/HAl/Ti-SBA-15 catalyst and, thus, promotes the HDN activity over both Ni-Mo and the Ti-synthesized catalysts employed in this study (Table 5). Several explanations for the direct C–N bond cleavage have been proposed. From a study of a series of substituted benzenes, Moreau et al. [82] suggested that the direct aromatic C–N bond cleavage takes place by nucleophilic substitution with a hydride ion. Iridium sites are capable to dissociate adsorbed H_2 . The direct denitrogenation reaction might proceed by partial hydrogenation of the aromatic ring, followed by hydrogenolysis of C–N bond over an acid site.

The adsorption strength and the rate of each step in the HDN of indole must be correlated with the nature of the catalyst. In a previous work we found that the iridium dispersion increases with the presence of titanium [44]. The dispersion of Ir species is still high with the incorporation of aluminum in the Ti-SBA-15, support, due to aluminum atoms serve as anchoring sites by strong interaction with Ir species. Ti-SBA-15 sample is a weak Lewis solid acid catalyst in comparison to mesoporous silica of Al/Ti-SBA-15. The ability to act as an acid of various solid acids follow the sequence: H-ZSM-5 > Al-SBA-3 > Al-SBA-15 > Al/Ti-SBA-15 > Ti-SBA-15 > TS-1 > TiO_2 [83–90]. The acid strength depends on the force with which attract electrons the conjugate base of acids sites. H-ZSM-5 catalyst has a great ability to incorporate aluminum in its structure and the consequent ability to generate more and strength acid sites. TS-1 catalyst has weakly acidic sites; the Ti^{4+} species within the MFI of TS-1 have less acidic than Al^{3+} species is H-ZSM-5. Siliceous SBA-15 has a low acidity, associated with a large number of silanol groups of the surface. The acid sites of Ti-SBA-15 are weak-medium related to the number of Ti^{4+} tetrahedral species [85]. Whereas Al containing-Ti-SBA-15 synthesized sample shows comparable acidic nature and strength than similar materials, without Ti [86,87], slightly higher acidity than Al-SBA-15 [88,89] and lower than Al-SBA-3 [90], because the conjugate base SBA-3 is a lower, but soft base than SBA-15. The acidity of the NiMo sulfides catalysts were studied by Zhang et al. [14]. They have proposed for HDN of nitrogen heterocycles over supported NiMo sulfides two major types of active sites: Hydrogenation sites, consisting of sulfur vacancies associated with Mo or Ni in Ni-Mo-S phase and C–N bond hydrogenolysis sites consisting of Brønsted acid centers associated with Mo atoms only. The adsorption and dissociation of an H_2S molecule can convert a sulfur vacancy to a Brønsted acid site and a sulfhydryl group (SH), but the adsorption is readily reversible if H_2S is removed from the reaction system. This was in agreement with some findings in the literature [91–96]. They also found that the Brønsted acid sites, which are responsible for C–N bond hydrogenolysis reactions are lost at 300 °C due to the easy desorption and reassociation of H^+ and SH^- to H_2S .

Although studies on the inhibition of NiMoS catalyst by nitrogen compounds have been reported, very few have precisely identified the dependency on the nature of site either Brønsted (–SH) or Lewis Mo or Ni, also called coordinatively unsaturated sites (CUS).

Nagai et al. [97] and La Vopa and Satterfield [71] have shown that, there was a correlation between the adsorption constant of the nitrogen molecules, representative of the inhibition strength, and their proton affinity. This correlation was explained by considering that the proton affinity was an indicator of the adsorption energy of the molecules on the Brønsted sites (sulfhydryl –SH groups) of the NiMoS active phases. Nevertheless, the kinetic studies conducted so far have not been able to determine adsorption constants associated with a given site. Thus, MoS_2 based catalysts exhibit a weak Brønsted acidity induced by the –SH groups, which can be probed by various basic molecules such as ammonia, pyridine and lutidine [92,98–101]. Furthermore, adsorption constant of *N*-molecules on Mo CUS is generally strong and even stronger than on the –SH

Table 7

TON of the samples at reaction time = 5.5 h.

Sample	HDN (mol%)	TON
Ir/SBA 15	19	9.4
Ir/Ti-SBA-15	71	299.8
Ir/F/Ti-SBA-15	27	130.0
Ir/HAl/Ti-SBA-15	92	390.0

group. Humbert et al. [102] using a DFT study found that interestingly, the calculated adsorption enthalpies on –SH group correlate reasonably well with gas phase proton affinities of the *N*-molecules.

This is in agreement with our finding that the more basic molecules present higher adsorption constant over the NiMo catalysts as well.

In order to find out if there is a direct correlation between Iridium dispersion and activity, is interesting to analyze the activity comparing the Turn Over Number (TON) (see Table 7). The turn over number was calculated considering the σ_m = cross-sectional area of active metal (0.074 nm²) and the active metal surface area per gram of sample, according H_2 chemisorption (Table 1). TON was calculated using the HDN conversion (number of denitrogenated molecules at 5.5 h of reaction time). The different values of TON suggest, that the higher conversion levels are more related to the nature of the catalytic centers involved in the reaction than to the Ir atoms dispersion. The higher value of TON for Ir/HAl/Ti-SBA-15 compared with Ir/Ti-SBA-15, despite of it slight lower dispersion is evidence than the iridium sites are different or another catalytic center is present in the aluminated sample. Both samples possess Lewis acid sites (Table 4) but in Ir/Ti-SBA-15 they are weak, only a few of them are present at 200 °C and disappear at 300 °C. Instead for Ir/HAl/Ti-SBA-15 the Lewis acid sites are stronger and remained after 300 °C. Since both catalysts are active, iridium sites and Lewis acid sites are believed to play an important role in the catalytic activity of Ir/Ti-SBA-15. This reinforces the idea that Brønsted + Lewis acidity, mainly Brønsted acidity of the aluminated sample is the main responsible for the higher HDN (C–N bond cleavage) activity. This also demonstrated the great influence of the support over the iridium actives species as we observed in the reducibility capacity by TPR and XPS characterizations.

The lower TON obtained for Ir/F/Ti-SBA-15 could be due that fluorine incorporation reduced surface area provoking some loss of structure and also diminished the dispersion of the crystallites. The remaining F may influence on the adsorption of the reactants, obtaining a worse catalytic performance. This may have hindered the complete reduction of IrO_2 on the surface, as the XPS analysis showed, and these species are not active in the hydrogenation or hydrogenolysis.

The iridium crystallites supported on HAl/Ti-SBA-15 were more active than those supported on the Ti-SBA-15, in spite of their similar average particle size. It is possible that the nanoparticles located on different supports have different properties due to the electron withdrawing by the support as we seen by the characterization techniques. This is more evident for the HDN reaction than for Indole hydrogenation where the differences are not so pronounced. In addition of the Brønsted acid site, we assume that Ir, obviously well dispersed and possibly in a reduced state, contributed significantly to C–N cleavage by a high hydrogenolytic activity, affecting in this way the overall rate of HDN. Ir acting as active hydrogen suppliers that could explain the activity of the samples without Brønsted acid sites and only weak Lewis acid sites are present.

In resume, the effect of Brønsted acidity weakly promotes the hydrogenation of indole, not influencing the conversion of OEA to EB and HIND to ECH and strongly promoting HDN of OEA to ECH.

4. Conclusion

The iridium catalysts prepared using the titanium-modified SBA-15 supports were very active for HDN of indole. These catalysts were more than six times more active than the silicious SBA-15 support and NiMo/Al₂O₃. Better selectivity to product without nitrogen atom is observed in the reaction with Ir/HAl/Ti-SBA-15, compared to that of reaction with Ir/Ti-SBA-15. It can be attributed to the presence of Bronsted sites derived from Al incorporation into the framework and the effect of the support changing the electronic environment of the iridium sites. This indicates that both titanium incorporation and alumination enhance hydrogenation of the aromatic ring of indole to indoline, and greatly promote HDN of OEA. Bronsted acidity increased selectivity to ECH in the HDN reaction. This observation is in line with the easier availability of hydrogen caused by the presence of Ir, which in the reduced form are well known as hydrogen activating agent providing active hydrogen for hydrogenation and hydrogenolysis. Fluorination did not improve HDN of indole.

Acknowledgments

The authors are very grateful to Drs. J.L. García Fierro, J.M. Martín for some characterization techniques performed in ICP-CSIC, Madrid and Dr. Gina Pecchi for N₂-Adsorption isotherms performed in Universidad de Concepcion, Chile.

We thank CONICET Argentina, PIP CONICET 11220120100218CO (2015–2017).

References

- [1] M.J. Girgis, B.C. Gates, *Ind. Eng. Chem. Res.* 30 (1991) 2021–2058.
- [2] E. Furimsky, F.E. Massoth, *Catal. Today* 52 (1999) 381–495.
- [3] F. Van Looij, P. Van der Laan, W.H.J. Stork, D.J. DiCamillo, J. Swain, *Appl. Catal. A* 170 (1998) 1–12.
- [4] G.C. Laredo, S. Leyva, R. Alvarez, M.T. Mares, J.J. Castillo, J.L. Cano, *Fuel* 81 (2002) 1341–1350.
- [5] M. Dorbon, C. Bernasconi, *Fuel* 68 (1989) 1068–1074.
- [6] H. Topsøe, B.S. Clausen, F.E. Massoth, *Hydrotreating Catalysis*, Springer, Berlin, 1996.
- [7] F.E. Massoth, K. Balusami, J. Shabtai, *J. Catal.* 122 (1990) 256–270.
- [8] M. Callant, P. Grange, K.A. Holder, B. Delmon, *Bull. Soc. Chim. Belg.* 104 (1995) 245–250.
- [9] L. Zhang, U.S. Ozkan, *Stud. Surf. Sci. Catal.* 101 (1996) 1223–1230.
- [10] C.N. Satterfield, *Heterogeneous Catalysis Industrial Practice*, 2nd ed., McGraw-Hill, New York, 1991, pp. 383–390 (Chapter 9).
- [11] G. Perot, *Catal. Today* 10 (1991) 447–451.
- [12] R. Prins, in: G. Ertl, H. Knözinger, J. Weitkamp (Eds.), *Handbook of Heterogeneous Catalysis*, 4, Wiley-VCH, Weinheim, 1997, pp. 1908–1920.
- [13] S.C. Kim, F.E. Massoth, *Ind. Eng. Chem. Res.* 39 (2000) 1705–1712.
- [14] L. Zhang, G. Karakas, U.S. Ozkan, *J. Catal.* 178 (1998) 457–465.
- [15] L.D. Rollmann, *J. Catal.* 46 (1977) 243–252.
- [16] M.V. Bhide, Ph.D. Dissertation, University of Delaware, Newark, 1979.
- [17] T.C. Ho, *Catal. Rev. Sci. Eng.* 30 (1988) 117–123.
- [18] O.Y. Gutierrez, T. Klimova, *J. Catal.* 281 (2011) 50–62.
- [19] F. Rashidi, T. Sasaki, A.M. Rashidi, A.N. Kharat, K.J. Jozani, *J. Catal.* 299 (2013) 321–335.
- [20] D. Laurenti, B. Phung-Ngoc, C. Roukoss, E. Devers, K. Marchand, L. Massin, L. Lemaitre, C. Legens, A. Quoineaude, M. Vrinat, *J. Catal.* 297 (2013) 165–175.
- [21] N. Kunisada, K.H. Choi, Y. Korai, I. Mochida, K. Nakano, *Appl. Catal. A* 269 (2004) 43–51.
- [22] J.C. Duchet, M.J. Tilliet, D. Cornet, L. Vivier, G. Perot, L. Bekakra, C. Moreau, G. Szabo, *Catal. Today* 10 (1991) 579–592.
- [23] J. Ramirez, S. Fuentes, G. Diaz, M. Vrinat, M. Breyse, M. Lacroix, *Appl. Catal.* 52 (1989) 211–224.
- [24] J. Escobar, M.C. Barrera, J.A.D. Reyes, J.A. Toledo, V. Santes, J.A. Colin, *J. Mol. Catal. A* 287 (2008) 33–40.
- [25] L. Kaluza, M. Zdrzil, *Collect. Czech. Chem. Commun.* 73 (2008) 945–955.
- [26] D. Trong On, D. Desplandier-Giscard, C. Danumah, S. Kaliaguine, *Appl. Catal. A* 253 (2003) 545–602.
- [27] K.C. Mouli, K. Soni, A. Dalai, J. Adjaye, *Appl. Catal. A* 404 (2011) 21–29.
- [28] G. Murali Dhar, G.M. Kumaran, M. Kumar, K.S. Rawat, L.D. Sharma, B.D. Raju, K.S. Rama Rao, *Catal. Today* 99 (2005) 309–314.
- [29] K. Soni, B.S. Rana, A.K. Sinha, A. Bhaumik, M. Nandi, M. Kumar, G.M. Dhar, *Appl. Catal. B* 90 (2009) 55–63.
- [30] S. Garg, T. Bhaskar, K. Soni, G.M. Kumaran, A. Muto, Y. Sakata, G. MuraliDhar, *Chem. Commun.* (2008) 5310–5311.
- [31] N. Kostova, A. Spojakina, K. Jiratoval, O. Solcova, L. Dimitrov, L. Petrov, *Catal. Today* 65 (2001) 217–223.
- [32] O.Y. Gutierrez, D. Valencia, G.A. Fuentes, T. Klimova, *J. Catal.* 249 (2007) 140–153.
- [33] G.M. Kumaran, S. Garg, K. Soni, M. Kumar, L.D. Sharma, G.M. Dhar, K.S.R. Rao, *Appl. Catal. A* 305 (2006) 123–129.
- [34] K. Soni, P.E. Boahene, K. Chandra Mouli, A.K. Dalai, J. Adjaye, *Appl. Catal. A* 398 (2011) 27–36.
- [35] K. Romero-Moreno, E. Leocadio-Cerón, G. Fuentes-Zurita, T. Klimova-Berestneva, *Rev. Mex. Ing. Quím.* 5 (2006) 179–187.
- [36] T. Klimova, E. Rodriguez, M. Martinez, J. Ramirez, *Microporous Mesoporous Mater.* 44–45 (2001) 357–365.
- [37] A.B. Dongil, C. Rivera-Cárcamo, L. Pastor-Pérez, A. Sepúlveda-Escribano, P. Reyes, *Catal. Today* 249 (2015) 72–78.
- [38] Z. Vit, *Appl. Catal. A* 322 (2007) 142–151.
- [39] H.T. Hwang, J.R. Martinelli, R. Gounder, A. Varma, *Chem. Eng. J.* 288 (2016) 758–769.
- [40] A. Infantes-Molina, A. Romero-Pérez, E. Finocchio, G. Busca, A. Jiménez-López, E. Rodríguez-Castellón, *J. Catal.* 305 (2013) 101–117.
- [41] D. Gulkova, Y. Yoshimura, Z. Vit, *Appl. Catal. B* 87 (2009) 171–180.
- [42] Z. Vit, D. Gulková, L. Kaluza, M. Zdrzil, *J. Catal.* 232 (2005) 447–455.
- [43] J. Cinibulk, Z. Vit, *Appl. Catal. A* 204 (2000) 107–116.
- [44] B.C. Ledesma, V.A. Valles, L.P. Rivoira, M.L. Martinez, O.A. Anunziata, A.R. Beltramone, *Catal. Lett.* 144 (2014) 783–795.
- [45] V.A. Vallés, G.S. Balangero Bottazzi, M.L. Martínez, M.B. Gómez Costa, O.A. Anunziata, A.R. Beltramone, *Ind. Eng. Chem. Res.* 51 (21) (2012) 7185–7195.
- [46] V.A. Valles, B.C. Ledesma, L.P. Rivoira, J. Cussa, Oscar A. Anunziata, A.R. Beltramone, *Catal. Today* (2016), <http://dx.doi.org/10.1016/j.cattod.2015.07.018> (in press) 08/2015.
- [47] W.H. Zhang, J. Lu, B. Han, M. Li, J. Xiu, Y.P. Ying, C. Li, *Chem. Mater.* 14 (2002) 3413–3421.
- [48] Zhao Li, Jiaguo Yu, *J. Colloid Interface Sci.* 304 (2006) 84–91.
- [49] G. Petrini, A. Cesana, G.F. De Alberti, G. Genoni, M. Leofanti, M. Padovan, G. Paparatto, P. Roffia, *Stud. Surf. Sci. Catal.* 68 (1991) 761–766.
- [50] Z. Luan, E.M. Maes, P.A.W. Van der Heide, D. Zhao, R.S. Czernuszewicz, L. Kevan, *Chem. Mater.* 11 (1999) 3680–3686.
- [51] S.Y. Balaji, J. Raman Spectrosc. 37 (2006) 1416–1422.
- [52] P. Reyes, M.C. Aguirre, G. Pecchi, J.L.G. Fierro, *J. Mol. Catal. A* 164 (1–2) (2000) 245–251.
- [53] H. Tian, T. Zhang, X. Sun, D. Liang, L. Li, *Appl. Catal. A* 210 (1–2) (2001) 55–62.
- [54] V.V. Atuchin, V.G. Kesler, N.V. Pervukhina, Z. Zhang, *J. Electron. Spectrosc. Relat. Phenom.* 152 (12) (2006) 18–24.
- [55] J. Klinowski, *Ann. Rev. Mater. Sci.* 18 (1988) 189–218.
- [56] T. Barzetti, E. Selli, D. Moscotti, L. Forni, *J. Chem. Soc. Faraday Trans. 92* (1996) 1401–1407.
- [57] T.R. Hughes, H.M. White, *J. Phys. Chem.* 71 (1967) 2192–2201.
- [58] M.C. Carrión, B.R. Manzano, F.A. Jalón, I. Fuentes-Perujo, P. Maires-Torres, E. Rodríguez-Castellón, A. Jiménez-López, *Appl. Catal. A* 288 (2005) 34–42.
- [59] D.J. Ostgard, L. Kustov, K.R. Poeppelmeier, W.M.H. Sachtler, *J. Catal.* 133 (1992) 342–357.
- [60] S. Subramanian, J.A. Schwarz, *Appl. Catal.* 68 (1991) 131–147.
- [61] P. Zeuthen, P. Stolze, U.B. Pedersen, *Bull. Soc. Chim. Belg.* 96 (1987) 985–995.
- [62] J. Shabtai, G. Que, K. Balusami, N.K. Nag, F.E. Massoth, *J. Catal.* 113 (1988) 206–219.
- [63] W.V. Steele, R.D. Chirico, *Topical Report for US DOE, Fossil Energy, Contract No. 22–83FE60149, NIPER 379, 1988.*
- [64] J.L. Olive, S. Biyoko, C. Moulinas, P. Geneste, *Appl. Catal.* 19 (1985) 165–174.
- [65] L. Zhang, U.S. Ozkan, *Stud. Surf. Sci. Catal.* 106 (1997) 69–82.
- [66] E.O. Odeunmi, D.F. Ollis, *J. Catal.* 80 (1983) 76–89.
- [67] A. Bunch, L. Zhang, G. Karakas, U.S. Ozkan, *Appl. Catal. A* 190 (2000) 51–60.
- [68] G. Adamskia, K. Dyrek, A. Kotarba, Z. Sojka, C. Sayag, G. Djéga-Mariadassou, *Catal. Today* 90 (2004) 115–119.
- [69] G.C. Laredo, E. Altamirano, J.A. De los Reyes, *Appl. Catal. A* 242 (2003) 311–320.
- [70] G.C. Laredo, E. Altamirano, J.A. De los Reyes, *Appl. Catal. A* 243 (2003) 207–214.
- [71] V. Lavolpa, C. Satterfield, *J. Catal.* 110 (1988) 375–387.
- [72] C.N. Satterfield, M. Modell, J.F. Mayer, *AIChE J.* 21 (1975) 1100.
- [73] C.N. Satterfield, M. Modell, J.A. Wilkens, *Ind. Eng. Chem. Proc. Des. Dev.* 19 (1980) 154–160.
- [74] L. Qu, R. Prins, *Appl. Catal. A* 250 (2003) 105–115.
- [75] G.C. Hadjilouzou, J.B. Butt, J.S. Dranoff, *J. Catal.* 131 (1991) 545–572.
- [76] D. Dong, S. Jeong, F.E. Massoth, *Catal. Today* 37 (1997) 267–275.
- [77] B.D. Muegge, F.E. Massoth, *Stud. Surf. Sci. Catal.* 68 (1991) 297–304.
- [78] C.S. Kim, F.E. Massoth, *J. Catal.* 189 (2000) 70–78.
- [79] F. Ruetter, F.M. Poveda, A. Sierraalta, M. Sanchez, E.N. Rodriguez-Aria, *J. Mol. Catal.* 119 (1997) 335–348.
- [80] J.L. Portefaix, M. Cattenot, M. Gueriche, M. Breyse, *Catal. Lett.* 9 (1991) 127–132.
- [81] M. Jian, F. Kapteijn, R. Prins, *J. Catal.* 168 (1997) 491–500.
- [82] C. Moreau, J. Joffre, C. Saenz, J.C. Afonso, J.L. Portefaix, *J. Mol. Catal. A* 161 (2000) 141–147.
- [83] T. Suzuta, M. Toba, Y. Abe, Y. Yoshimura, *J. Am. Oil Chem. Soc.* 89 (2012) 1981–1989.

- [84] T. Mochizuki, S.Y. Chen, M. Toba, Y. Yoshimura, *Appl. Catal. B: Environ.* 146 (2014) 237–243.
- [85] S. Yuan Chen, T. Mochizuki, Y. Abe, M. Toba, Y. Yoshimura, *Appl. Catal. B: Environ.* 148–149 (2014) 344–356.
- [86] T. Klimova, J. Reyes, O. Gutiérrez, L. Lizama, *Appl. Catal. A: Gen.* 335 (2008) 159–171.
- [87] M. Boutros, T. Onfroy, P. Da Costa, *Catal. Lett.* 139 (2010) 50–55.
- [88] K. Jaroszewska, A. Masalska, K. Baczowska, J.R. Grzechowiak, *Catal. Today* 196 (2012) 110–118.
- [89] A. Medina Mendoza, M. Cortes-Jacome, J. Toledo-Antonio, C. Angeles-Chavez, E. Lopez-Salinas, I. Cuauhtemoc-Lopez, M. Barrera, J. Escobar, J. Navarrete, I. Hernandez, *Appl. Catal. B* 106 (2011) 14–25.
- [90] M.L. Martínez, M.B. Gómez Costa, G.A. Monti, O.A. Anunziata, *Microporous Mesoporous Mater.* 144 (2011) 183–190.
- [91] G.C. Hadjilouzou, J.B. Butt, J.S. Dranoff, *Ind. Eng. Chem. Res.* 31 (1992) 2503–2516.
- [92] N.Y. Topsøe, H. Topsøe, *J. Catal.* 84 (1983) 386–401.
- [93] S.H. Yang, C.N. Satterfield, *Ind. Eng. Chem. Process Des. Dev.* 23 (1984) 20–26.
- [94] I. Alstrup, I. Chorkendorff, R. Candia, B.S. Clausen, H. Topsøe, *J. Catal.* 7 (1982) 397–409.
- [95] H.G. McIlvried, *Ind. Eng. Chem. Process Des. Dev.* 10 (1971) 125–130.
- [96] M.J. Ledoux, *Appl. Catal.* 9 (1984) 31–40.
- [97] M. Nagai, T. Sato, A. Aiba, *J. Catal.* 97 (1986) 52–58.
- [98] A. Logadottir, P.G. Moses, B. Hinnemann, N.Y. Topsøe, K.G. Knudsen, H. Topsøe, J.K. Nørskov, *Catal. Today* 111 (2006) 44–51.
- [99] B. Temel, A.K. Tuxen, J. Kibsgaard, N.Y. Topsøe, B. Hinnemann, K.G. Knudsen, H. Topsøe, J.V. Lauritsen, F. Besenbacher, *J. Catal.* 271 (2010) 280–289.
- [100] N.Y. Topsøe, H. Topsøe, F.E. Massoth, *J. Catal.* 119 (1989) 252–255.
- [101] F. Maugé, J. Lamotte, N.S. Nesterenko, O. Manoilova, A.A. Tsyganenko, *Catal. Today* 70 (2001) 271–284.
- [102] S. Humbert, G. Izzet, P. Raybaud, *J. Catal.* 333 (2016) 78–93.